



Cite this: *Phys. Chem. Chem. Phys.*,  
2025, 27, 2444

# A new 3D metallic, ductile, and porous boron nitride as a promising anode material for sodium-ion batteries†

Wei Sun,<sup>a</sup> Qian Wang <sup>\*ab</sup> and Puru Jena <sup>b</sup>

We propose a new stable three-dimensional (3D) porous and metallic boron nitride anode material, named h-B<sub>10</sub>N<sub>12</sub>, with good ductility for sodium-ion batteries (SIBs). Based on first-principles calculations and a tight-binding model, we demonstrate that the metallicity originates from the synergistic contribution of the p-orbital of the sp<sup>2</sup>-hybridized B and N atoms, while the ductility is due to the unique configurations of B–B and N–N dimers in the structure. More importantly, this boron nitride allotrope exhibits a high reversible capacity of 582.21 mA h g<sup>-1</sup> in gravimetric density and 663.72 mA h cm<sup>-3</sup> in volumetric density, fast Na-ion transport dynamics with low energy barriers ranging from 0.06 to 0.12 eV, a small volume change of 2.77%, and a long cycle-life. This study not only expands the family of conventional boron nitride materials with new features, but also enriches the family of anode materials for SIBs with high performance.

Received 11th November 2024,  
Accepted 31st December 2024

DOI: 10.1039/d4cp04297b

rsc.li/pccp

## 1. Introduction

Fast-charging batteries for electric vehicles up to 80% capacity within 15 minutes are targeted by the US Advanced Battery Consortium. To achieve this goal, both ionically and electronically conductive anode materials are highly desirable.<sup>1,2</sup> Consequently, in recent years, great efforts have been devoted to design and synthesize porous and metallic anode materials composed of abundant, lightweight elements such as carbon, boron, and phosphorus. For instance, 3D conducting networks<sup>3,4</sup> composed of carbon nanotubes and nanofibers have been synthesized, showing rapid transport of electrons and Li ions in lithium-ion batteries (LIBs). A 3D metallic carbon allotrope, Hex-C<sub>18</sub>,<sup>5</sup> was theoretically designed that possesses a maximum specific capacity of 496 mA h g<sup>-1</sup> when served as an anode material for LIBs. 3D porous and metallic carbons, Hex-C<sub>558</sub><sup>6</sup> and Tet-C<sub>52</sub>,<sup>7</sup> respectively, composed of 5-5-8 nanoribbons and biphenylene-nanoribbons, exhibit high specific capacities of 591 mA h g<sup>-1</sup> and 458 mA h g<sup>-1</sup> with small volume expansions of 2.4% and 1.5%, respectively, for LIB anode materials. In addition to these electronically conducting porous carbon systems, boron-based conducting anodes for LIBs have also been explored for high

capacity, including the B<sub>4</sub> cluster-based H-boron<sup>8</sup> and borophene-nanoribbon-based 3D-β<sub>12</sub>-borophene.<sup>9</sup>

On the other hand, sodium-ion batteries (SIBs) have also attracted much attention recently, due to their abundance, cost-effectiveness, and high operating safety. However, the larger ionic radius of Na<sup>+</sup> compared to that of Li<sup>+</sup> makes most LIB anode materials unsuitable for SIBs.<sup>10</sup> Nowadays, many 2D materials are being explored for serving as SIB anode materials such as experimentally synthesized F-BNNS<sup>11</sup> and bilayer TZACOF,<sup>12</sup> and theoretically rationally designed p-BP,<sup>13</sup> while 3D anode materials are more practical in application. Hence, this has prompted numerous studies, particularly on 3D porous metallic carbon for SIB anodes. For instance, 3D porous and metallic honeycomb carbon hC28<sup>14</sup> was found to be a promising SIB anode candidate with a theoretical specific capacity of 717 mA h g<sup>-1</sup>. 3D porous and metallic penta-oC36<sup>15</sup> consisting of penta-graphene nanoribbons was reported to show an ultra-low diffusion energy barrier of 0.01 eV for Na ions. Recently, 3D porous and metallic HexC28 and HexC46<sup>16</sup> composed of arm-chair biphenylene-nanoribbons with different widths were proposed for SIBs with high capacities.

Because of their thermal stability and chemical inertness, boron nitrides, composed of the nearest neighbors of the carbon element in the periodic table, exhibit significant advantages over carbon materials for applications in electronic devices,<sup>17</sup> optoelectronic devices,<sup>18</sup> and extremely harsh environments.<sup>19</sup> We proposed the first 3D metallic BN in 2013.<sup>20</sup> Since then, several 3D metallic boron nitrides have been theoretically identified, including zeolite-like microporous (P-6M2)-BN and (IMM2)-BN,<sup>21</sup>

<sup>a</sup> School of Materials Science and Engineering, CAPT, Peking University, Beijing, 100871, China. E-mail: qianwang2@pku.edu.cn

<sup>b</sup> Department of Physics, Institute for Sustainable Energy and Environment, Virginia Commonwealth University, Richmond, VA, 23284, USA

† Electronic supplementary information (ESI) available. See DOI: <https://doi.org/10.1039/d4cp04297b>

h-BN nanoribbon-based HCBN-1 and HCBN-2,<sup>22</sup> *M*-BN,<sup>23</sup>  $B_xN_{x+1}$ ,<sup>24</sup> and penta- $B_4N_7$ .<sup>25</sup> However, there have been no reports so far on the study of using 3D metallic boron nitrides as the anode materials for SIBs, although some semiconducting porous boron nitrides for metal-ion batteries have been recently explored.<sup>26,27</sup> In addition, the ductility of anode materials is important to maintain good contact with the electrolyte interface and extend the cycling lifespan. However, most of the reported metallic boron nitrides are brittle.<sup>20,23–26</sup> Therefore, for bridging this gap, we propose a new 3D boron nitride allotrope that integrates advantages of metallicity, ductility and porosity as a promising anode material for SIBs.

## 2. Computational methods

Our calculations are on the basis of density functional theory (DFT) as coded in the Vienna *ab initio* simulation package (VASP).<sup>28</sup> Ion–electron interactions are treated using the projector augmented wave (PAW) pseudopotential<sup>29,30</sup> with a kinetic energy cutoff of 600 eV. The exchange–correlation interactions of electrons are accounted for by using the generalized gradient approximation (GGA)<sup>31</sup> and the Perdew–Burke–Ernzerhof (PBE) functional.<sup>32</sup> For calculating the electronic band structure, a more accurate Heyd–Scuseria–Ernzerhof (HSE06) hybrid functional<sup>33,34</sup> is used. The convergence thresholds for total energy and force are set as  $10^{-8}$  eV and  $10^{-6}$  eV  $\text{\AA}^{-1}$ , respectively. The first Brillouin zone is represented by using a  $3 \times 3 \times 7$  *k*-mesh within the Monkhorst–Pack scheme.<sup>35</sup> To check the dynamic stability, the phonon frequencies with the same convergence criteria are calculated utilizing the finite displacement method<sup>36</sup> embedded in the phonopy package.<sup>37</sup> To verify the thermal stability, *ab initio*

molecular dynamics (AIMD)<sup>38</sup> simulations are carried out in the frame of the canonical ensemble using a Nose–Hoover thermostat<sup>39</sup> controlling the temperature. The energy–strain method<sup>40</sup> is used to obtain elastic constants that ensure mechanical stability. To explore the origin of metallicity, a tight-binding (TB) Hamiltonian is generated by projecting the Bloch states onto the maximally localized Wannier functions using the WANNIER90 package.<sup>41</sup> The effect of van der Waals interactions on the adsorption and diffusion behavior of Na ions and the electrochemical properties of the anode are studied with the PBE-D2 functional.<sup>42</sup> The climbing-image nudged elastic band (CI-NEB) method<sup>43</sup> is utilized for the calculations of diffusion energy barrier profiles.

## 3. Results and discussion

### 3.1 Structure and stability

Our design starts from using the ground state of pentagonal boron nitride clusters<sup>44</sup> as the building block. Through the analysis of previous related research work, we found that  $sp^3$ -hybridized B atoms are more suitable for cross-linkers rather than  $sp^3$ -hybridized N, like in the cases of 2D penta-BN, penta-BN<sub>2</sub>, penta-B<sub>3</sub>N<sub>3</sub>, and 3D penta-B<sub>4</sub>N<sub>7</sub>.<sup>25,45,46</sup> Thus, we choose the ground state of the pentagonal B<sub>3</sub>N<sub>2</sub> cluster and utilize the  $sp^3$ -hybridized B atoms as the cross-linker to balance the ratio of B and N elements for stabilizing the 3D architecture. The corresponding building blocks and assembling process are schematically plotted in Fig. 1(a). The constructed 3D structure contains 10 B and 12 N atoms in its optimized unit cell with the No. 191 space group *P6/mmm*, belonging to hexagonal lattice

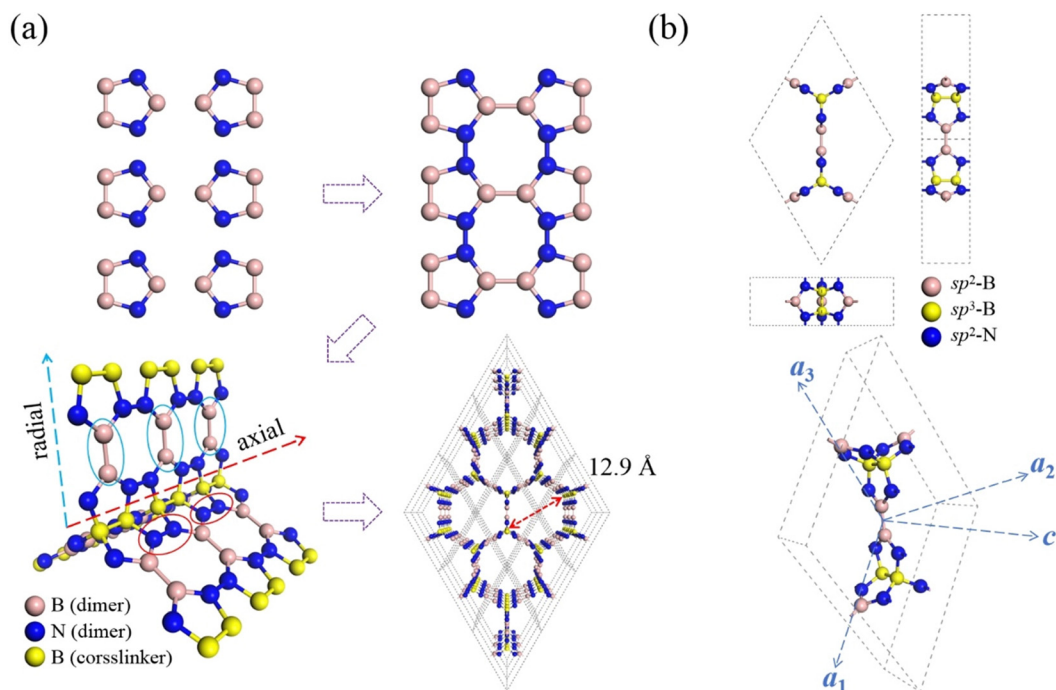


Fig. 1 (a) Schematic diagram of the building block and the assembly process of  $h\text{-B}_{10}\text{N}_{12}$  with the  $sp^3$ -hybridized B atoms (in yellow) as the cross-linkers. (b) Orthographic and perspective views of the optimized  $h\text{-B}_{10}\text{N}_{12}$ .

symmetry, thus termed h-B<sub>10</sub>N<sub>12</sub>, as shown in Fig. 1(b). The optimized lattice constants are  $a = b = 11.19 \text{ \AA}$ ,  $c = 3.72 \text{ \AA}$ ,  $\alpha = \beta = 90^\circ$ , and  $\gamma = 120^\circ$ . In this structure, N atoms are on the equivalent Wyckoff position of 12o (0.179586, 0.589793, and 0.182614) while B atoms occupy two chemically nonequivalent Wyckoff positions, which are 6m (0.086534, 0.543267, and 0.5) and 4h (0.333333, 0.666667, and 0.292326). Due to the porosity and the 1D hexagonal channels with a 12.9 Å diameter along the axial direction, h-B<sub>10</sub>N<sub>12</sub> possesses a low mass density of  $1.14 \text{ g cm}^{-3}$ , which is comparable to those of ultra-light super-(BN)<sub>16</sub> ( $0.78 \text{ g cm}^{-3}$ )<sup>47</sup> and porous 3D-B<sub>2</sub>N<sub>2</sub> ( $1.39 \text{ g cm}^{-3}$ ).<sup>27</sup>

Next, we examine the thermodynamic, dynamical, thermal, and mechanical stability of h-B<sub>10</sub>N<sub>12</sub>. We propose a synthesis pathway shown in Fig. S1 in the ESI,<sup>†</sup> similar to that used for the successful synthesis of the 3D graphene nanoribbon framework<sup>48</sup> *via* the bottom-up molecular assembly. To check the energetics of the formation process, we calculate the change of total free energy in assembling and found that the energy cost of forming a trifoliate-unit *via* sp<sup>3</sup>-hybridizing B is 0.27 eV per atom, while the formation of new N-N and B-B bond releases  $-0.48 \text{ eV}$  per atom in total. In addition, to check the thermodynamic stability, we also calculate the formation energy by considering the potential energy of each individual atom in its most stable conditions, which is found to be  $-0.033 \text{ eV}$  per atom. The negative value implies that the synthesis of h-B<sub>10</sub>N<sub>12</sub> is energetically favorable. To examine its dynamical stability, we calculate the phonon band spectrum using a  $1 \times 1 \times 3$  supercell with the aim of minimizing the constraint of the periodic boundary conditions. As shown in Fig. 2(a), there are no any imaginary frequencies existing in the entire first Brillouin zone, proving the dynamical stability of h-B<sub>10</sub>N<sub>12</sub>. To check the thermal stability, we conduct the AIMD simulations for 10 ps heating time by using 1 fs as the time step within the temperature ranging from 300 K to 1000 K at an interval of 100 K. The calculated total potential energies and the geometry at the end of the simulation at 1000 K are presented in Fig. 2(b), showing that the potential energy fluctuates around a certain constant value in the entire process, while the atomic configuration remains nearly intact, implying that h-B<sub>10</sub>N<sub>12</sub> possesses thermal stability up to 1000 K.

The mechanical stability of h-B<sub>10</sub>N<sub>12</sub> is investigated based on the calculation of its elastic stiffness matrix. For a hexagonal

crystal lattice, the five independent elastic constants are calculated to be  $C_{11} = 91.10 \text{ GPa}$ ,  $C_{12} = 81.94 \text{ GPa}$ ,  $C_{13} = 35.18 \text{ GPa}$ ,  $C_{33} = 423.32 \text{ GPa}$ , and  $C_{44} = 49.70 \text{ GPa}$ , which meet the corresponding Born–Huang criteria,<sup>49</sup> namely,  $C_{11} > |C_{12}|$ ,  $2C_{13}^2 < C_{33}(C_{11} + C_{12})$ ,  $C_{44} > 0$ , indicating that h-B<sub>10</sub>N<sub>12</sub> is mechanically stable.

### 3.2 Mechanical and electronic properties

The mechanical properties of h-B<sub>10</sub>N<sub>12</sub> are further studied by calculating its bulk modulus  $B$ , shear modulus  $G$ , and Poisson ratio  $\nu$  within the framework of the Voigt–Reuss–Hill approximation.<sup>50,51</sup> From the calculated results and related comparisons presented in Table 1, one can see that h-B<sub>10</sub>N<sub>12</sub>'s capability of resisting external stress and deformation is comparable to some previously studied hexagonal carbon allotropes, exhibiting good mechanical performance. Next, we explore the mechanical anisotropy by calculating the Young modulus  $E$  in different crystal directions based on the following equation:<sup>52</sup>

$$E(\mathbf{n}) = \frac{1}{s_{11}(1 - n_3^2)^2 + s_{33}n_3^4 + (2s_{13} + s_{44})(1 - n_3^2)n_3^2} \quad (1)$$

Here,  $s_{11}$ ,  $s_{13}$ ,  $s_{33}$  and  $s_{44}$  are the non-zero constants in the corresponding elastic compliance matrix, and  $\mathbf{n} = (n_1, n_2, n_3)$  is the unit vector along a specific stretching direction. The calculated Young modulus in the radial direction is 17.36 GPa, much lower than the value of 409.00 GPa in the axial direction, suggesting that h-B<sub>10</sub>N<sub>12</sub> has high mechanical anisotropy. This is further confirmed by the plotted 3D schematic diagram for the bulk modulus  $B$  and shear modulus  $G$ , as shown in Fig. 2(c). In addition, we further evaluate the ductility of this structure using Pugh's criteria<sup>53</sup> that classify materials to be ductile when their Poisson's ratio is  $\nu > 0.26$  and the ratio of shear modulus to bulk modulus is  $G/B < 0.57$ . The calculated results are  $\nu = 0.35$  and  $G/B = 0.34$ , implying the good ductility of this system. It should be noted that the exhibited intrinsic ductility is rarely seen in boron nitride materials (see Table S1, ESI<sup>†</sup>). The ductility of h-B<sub>10</sub>N<sub>12</sub> can be attributed to the orderly arrangement of N–N and B–B dimers. Different from many previously reported 3D boron nitrides containing a series of B–N dimers,<sup>20,54</sup> in this structure, B and N atoms are separated into two types of dimers where the N–N dimers with strong bonding align in the axial direction to provide the strength while the sp<sup>2</sup>-hybridized B–B dimers along

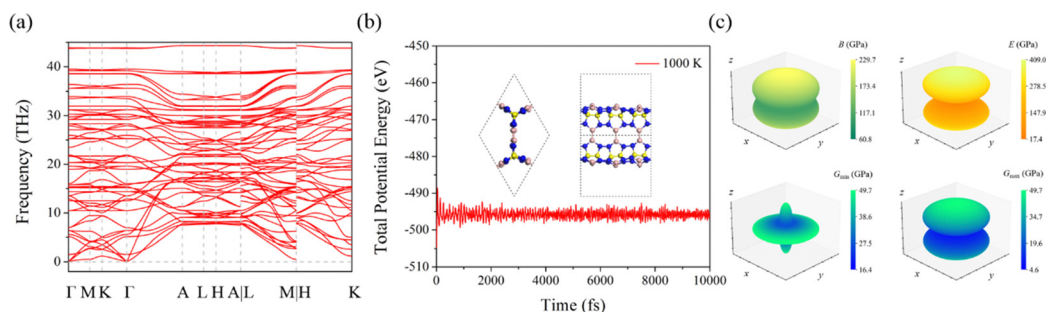


Fig. 2 (a) Phonon spectrum and (b) variation of the total potential energy with the simulation time at 1000 K, and the final geometry shown in the insets of h-B<sub>10</sub>N<sub>12</sub>. (c) 3D schematic diagram of mechanical properties including the bulk modulus  $B$ , Young modulus  $E$ , and shear modulus  $G$  for h-B<sub>10</sub>N<sub>12</sub>.

**Table 1** Calculated bulk modulus  $B$  (in GPa), shear modulus  $G$  (in GPa), Poisson's ratio  $\nu$ , and Young's modulus  $E(\mathbf{n})$  (in GPa) for h-B<sub>10</sub>N<sub>12</sub> compared with some other hexagonal carbon systems

	h-B <sub>10</sub> N <sub>12</sub>	Hex-C <sub>568</sub> <sup>55</sup>	Hex-C <sub>57</sub> <sup>56</sup>
$B_{\text{H}}$	90.8	92.1	101.2
$G_{\text{H}}$	30.7	27.7	32.4
$\nu_{\text{H}}$	0.35	0.36	0.36
$E(\mathbf{a}) = E(\mathbf{b})$	17.4	4.0	10.7
$E(\mathbf{c})$	409.0	377.6	377.8

the radial directions offer the flexibility, as depicted in Fig. 1(a). Therefore, the effective synergy of vertically arranged N–N and B–B dimers endows the structure with both high strength and intrinsic ductility.

To study the electronic properties of h-B<sub>10</sub>N<sub>12</sub>, we first calculate the electronic band structure at the HSE06 level, and the results are plotted in Fig. 3(a), which shows that the partially occupied bands pass through the Fermi energy level along the  $\Gamma$ –A path, suggesting that h-B<sub>10</sub>N<sub>12</sub> is intrinsically metallic. The partial density of states (PDOS) of the s- and p-orbitals of B and N atoms indicate that the intrinsic metallicity originates from a combination of the p-orbitals of sp<sup>2</sup>-hybridized B and N atoms. Different from the individual contribution of sp<sup>2</sup>-hybridized B or N atoms in the previously reported cases like T-B<sub>3</sub>N<sub>3</sub><sup>20</sup> or penta-B<sub>4</sub>N<sub>7</sub>,<sup>25</sup> the pentagonal boron nitride rings in this structure combines the contribution of sp<sup>2</sup>-hybridized B and N together, further enhancing its metallicity. In addition, we also construct a TB model with the maximally localized Wannier functions<sup>41</sup> by projecting the p-orbitals of sp<sup>2</sup>-hybridized B and N atoms with the Hamiltonian as given in the following:

$$H = \varepsilon_0 \sum_i c_i^\dagger c_i + \sum_{ij} (t_{ij} c_i^\dagger c_j + \text{H.c.}). \quad (2)$$

Here,  $c_i^\dagger$ ,  $c_i$ ,  $\varepsilon_0$  and  $t_{ij}$  are for the electronic creation and annihilation operators of the p-orbital at site  $i$ , the on-site energy and the hopping integral for describing electrons moving from one site to another, respectively. The results are presented in Fig. 3(a), which shows that the main feature of the electronic energy band near the Fermi level agrees well with that calculated from our DFT method, further validating the metallicity originating from the combined contributions of the p-orbitals of the

sp<sup>2</sup>-hybridized B and N atoms. This is different for other metallic boron nitrides where metallicity originates either from B atoms (T-B<sub>3</sub>N<sub>3</sub><sup>20</sup>) or from N atoms (penta-B<sub>4</sub>N<sub>7</sub><sup>25</sup>). Furthermore, we study the electron localization function (ELF)<sup>57</sup> of h-B<sub>10</sub>N<sub>12</sub> for visualizing the detailed electronic distribution and internal conducting channels. As plotted in Fig. 3(b), the charge density distributions in the two selected (11 $\bar{2}$ 0) and (1 $\bar{1}$ 00) lattice planes show that the delocalized electrons form conducting channels along the [0001] direction resulting from the combined contributions of the p-orbitals of sp<sup>2</sup>-hybridized B and N atoms.

### 3.3 Application as an SIB anode material

It should be noted that h-B<sub>10</sub>N<sub>12</sub> possesses all the desired properties for an outstanding anode material of SIBs, where the geometrical porosity can provide the needed storage space, the mechanical ductility can provide good contact with the solid electrolyte, and intrinsic metallicity can facilitate rate performance. Therefore, we carry out a thorough study of the electrochemical properties including maximal theoretical reversible capacity, average open-circuit voltage, diffusion energy barrier, and volume change during the charge–discharge process.

To explore preferable adsorption sites for Na atoms on the h-B<sub>10</sub>N<sub>12</sub> substrate, we first introduce Na atoms at various sites in the 1 × 1 × 3 supercell of h-B<sub>10</sub>N<sub>12</sub> so as to avoid the interaction between neighboring atoms. As presented in Fig. 4(a), three types of nonequivalent sites are taken into consideration, including the bonds' bridge site (B), the atomic rings' hollow site (H), and the atoms' top site (T). After full geometry optimization of all these adsorption configurations, we found that the Na atoms at different candidate sites move to three preferred adsorption sites, labeled as B1, H1, and H3 in Fig. 4(a). To further study the binding strength, we analyze the binding energy  $E_b$  defined as

$$E_b = (E_{\text{Na}_x-\text{hB}_{10}\text{N}_{12}} - E_{\text{hB}_{10}\text{N}_{12}} - x\mu_{\text{Na}})/x. \quad (3)$$

Here,  $E_{\text{Na}_x-\text{hB}_{10}\text{N}_{12}}$  ( $E_{\text{hB}_{10}\text{N}_{12}}$ ),  $\mu_{\text{Na}}$  and  $x$  are the total energy of the substrate with (without) the adsorbed Na atoms, the energy of a Na atom in the bulk phase, and the total number of Na atoms in the supercell, respectively. The corresponding values for B1, H1, and H3 adsorption sites are  $-0.99$ ,  $-0.90$ , and  $-0.92$  eV, respectively, implying that B1 is energetically the most

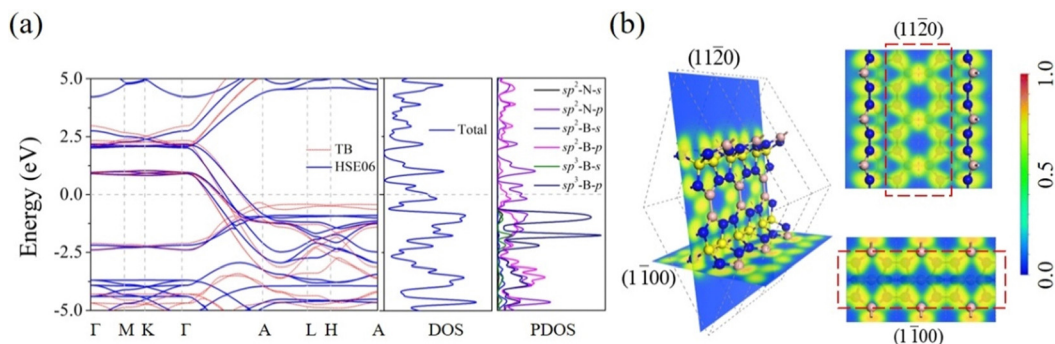


**Fig. 3** (a) Electronic band structures of h-B<sub>10</sub>N<sub>12</sub> at the HSE06 level and that obtained from the TB model, and PDOS at the HSE06 level for the s and p orbitals of different hybridized B and N atoms. (b) ELF distributions on the selected (11 $\bar{2}$ 0) and (1 $\bar{1}$ 00) of h-B<sub>10</sub>N<sub>12</sub>.

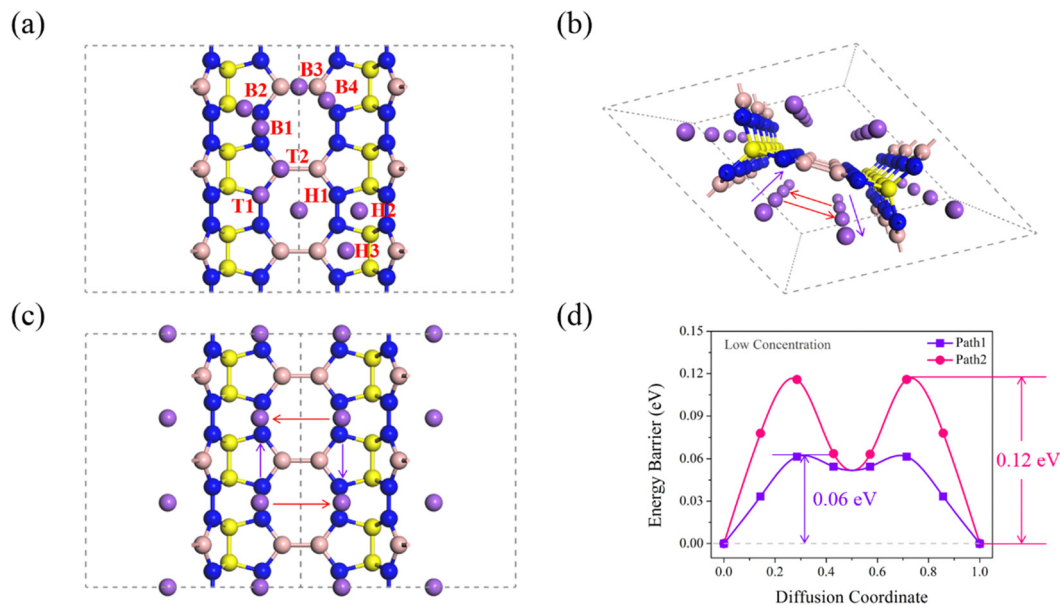


Fig. 4 (a) Potential nonequivalent single Na atom adsorption sites. (b) Perspective and (c) orthographic views of the full adsorption configuration with potential diffusion pathways for Na-ions in h-B<sub>10</sub>N<sub>12</sub> and (d) corresponding diffusion energy barriers.

favorable adsorption site for a single Na atom. Next, we carry out the Bader charge analysis<sup>58</sup> to evaluate the charge transfer from the Na atom to the h-B<sub>10</sub>N<sub>12</sub> substrate upon adsorption. The calculated value is 0.88  $|e|$ , implying that the Na's ionization process is nearly complete which benefits the battery operation.

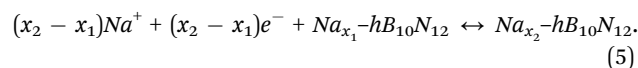
The maximal theoretical capacity of h-B<sub>10</sub>N<sub>12</sub> is calculated by gradually intercalating Na atoms on these favorable adsorption sites and its equivalents. Meanwhile, we calculate the energy of the corresponding system until reaching an unfavorable state. In addition, we distribute the Na atoms following the geometrical symmetry and keep a distance between neighboring ones to avoid clustering. The perspective and orthographic views of the final fully adsorbed configuration with one unit cell accommodating 6 Na atoms are presented in Fig. 4(b) and (c). The corresponding maximum theoretical gravimetric capacity ( $C_M$ ) and volumetric capacity ( $C_V$ ) are evaluated based on the following formulae:

$$C_M = \frac{n_m F}{M}, \quad C_V = \frac{n_m F}{V}. \quad (4)$$

Here,  $n_m$  is the maximum adsorption number of Na ions,  $F$  is the Faraday constant with a value of 26.8 A h mol<sup>-1</sup>, and  $M$  and  $V$  are the mass and volume of the h-B<sub>10</sub>N<sub>12</sub> substrate, respectively. The gravimetric and volumetric capacities are found to be 582.21 mA h g<sup>-1</sup> and 663.72 mA h cm<sup>-3</sup>, respectively, far exceeding that of many experimentally synthesized traditional metal-ion battery anode materials such as graphite (35 mA h g<sup>-1</sup>)<sup>59</sup> and hard carbon (230 mA h g<sup>-1</sup>).<sup>60</sup> Such a maximal theoretical capacity is comparable to many previously reported 3D boron nitride SIB anodes such as lz1-BN (539.94 mA h g<sup>-1</sup>)<sup>26</sup> and 3D-B<sub>2</sub>N<sub>2</sub> (599.90 mA h g<sup>-1</sup>),<sup>27</sup> and higher than that of some boron-nitride-based 3D light SIB anodes including h-BC<sub>2</sub>N (549 mA h g<sup>-1</sup>)<sup>61</sup> and 3D-Si<sub>2</sub>BN (341.61 mA h g<sup>-1</sup>).<sup>62</sup>

To assess the rate capability, we examine the diffusion energy barriers of all the potential ionic migration paths at low and high Na concentrations by utilizing the CI-NEB method.<sup>43</sup> Considering the symmetry of the substrate structure and distribution of adsorption sites, two potential Na ions' migration paths are found for diffusion as plotted in Fig. 4(b) and (c). One of these is along the 1D axial pathway, and the other is the exchange between neighboring conducting channels. Thus, all diffusion results can be achieved by combining these two migration paths. The Na-ion diffusion is significantly affected by the porosity of h-B<sub>10</sub>N<sub>12</sub>, where the 1D channels along the axial direction serve as "path 1" (in purple), allowing direct transport of Na ions, while the large pores with a diameter of 12.9 Å form "path 2" (in red) for fast diffusion of Na ions, as shown in Fig. 4(b) and (c). As the corresponding profiles plotted in Fig. 4(d), the calculated energy barriers range from 0.06 to 0.12 eV, which is comparable to that of 3D-B<sub>2</sub>N<sub>2</sub> (0.04–0.08 eV)<sup>27</sup> and much lower than those of lz1-BN (0.27 eV),<sup>26</sup> h-BC<sub>2</sub>N (0.35 eV),<sup>61</sup> and 3D-Si<sub>2</sub>BN (0.19–0.21 eV).<sup>62</sup> According to the explanation of the Arrhenius equation,<sup>63</sup>  $D \propto \exp\left(-\frac{E_{\text{barrier}}}{k_B T}\right)$ , the lower energy barrier leads to the higher diffusion constant  $D$ . Here,  $E_{\text{barrier}}$ ,  $k_B$ , and  $T$  refer to the energy barrier, Boltzmann constant, and temperature, respectively. Hence, the system exhibits fast kinetics of Na-ion migration and also possesses high ionic conductivity. The results of diffusion energy barriers in the high concentration are presented in Fig. S2 (ESI†).

To further determine the specific configuration of intermediate states under different concentrations, we analyze the half-cell reaction *versus* Na/Na<sup>+</sup>:



By employing the Ewald energy method described in pymatgen,<sup>64,65</sup> we produce five groups of nonequivalent configurations with the Na-ion concentrations ranging from  $x = 0.167$  to  $0.833$  with an interval of  $0.167$ . Then, after full optimization of all the possible structures and the comparison of the corresponding total energies, we choose the energetically most favorable configuration as the ground state structure for each concentration. As shown in Fig. S3 (ESI<sup>†</sup>), we found that these Na ion-intercalated intermediate configurations are all almost intact without obvious distortion, indicating the working cycling stability of the h-B<sub>10</sub>N<sub>12</sub> anode during the charging/discharging process.

To further examine the thermodynamic stability, we study the equilibrium convex hull based on the calculated formation energy  $E_f$  formulated as:

$$E_f = E_{\text{Na}_{x_1}\text{-hB}_{10}\text{N}_{12}} - (1 - x)E_{\text{hB}_{10}\text{N}_{12}} - xE_{\text{Na-hB}_{10}\text{N}_{12}}. \quad (6)$$

Here,  $E_{\text{Na}_{x_1}\text{-hB}_{10}\text{N}_{12}}$ ,  $E_{\text{hB}_{10}\text{N}_{12}}$ , and  $E_{\text{Na-hB}_{10}\text{N}_{12}}$  are the total energies of the selected energetically most favorable Na-adsorbed structure in different concentrations of  $x$  ranging between 0 and 1, respectively. From the results presented in Fig. 5(a), we find that those selected intermediate states at concentrations of  $x = 0.056$ ,  $0.167$ , and  $0.833$  are thermodynamically stable as determined by the convexity of the hull diagram. On this basis and the binding energy eqn (3), we can further calculate the respective adsorption energy and plot its variation with concentration. As shown in Fig. 5(b), one can see that the binding strength tends to become weaker gradually as the ion concentration increases. This results from the strengthened Coulomb repulsion among a large number of Na ions, effectively avoiding the formation of Na clusters to some extent.

Next, we further estimate the average open-circuit voltage  $V$  defined as

$$V \approx \frac{E_{\text{Na}_{x_1}\text{-hB}_{10}\text{N}_{12}} - E_{\text{Na}_{x_2}\text{-hB}_{10}\text{N}_{12}} + (x_2 - x_1)\mu_{\text{Na}}}{x_2 - x_1}. \quad (7)$$

Here,  $E_{\text{Na}_{x_1}\text{-hB}_{10}\text{N}_{12}}$  and  $E_{\text{Na}_{x_2}\text{-hB}_{10}\text{N}_{12}}$  are the total energies of the Na ion adsorbed structure with concentrations of  $x_1$  and  $x_2$ , respectively. In Fig. 5(c), we plot the voltage profile within the half-cell model and found that the plateaus gradually decrease while the values always remain positive through the entire Na-ion

concentration region. It suggests that this half-cell reaction will occur spontaneously until the end and the maximal theoretical capacity can be achieved reversibly. Then we evaluate the average open-circuit voltage by calculating the numerical average of all the voltage values on the curve. The result is found to be  $0.58$  V, which is comparable to that of the light carbon anode tC<sub>24</sub> ( $0.54$  V)<sup>66</sup> and much lower than that of the silicon anode ISN ( $1.35$  V).<sup>67</sup> The low voltage of the h-B<sub>10</sub>N<sub>12</sub> anode favors the high energy density.

To examine the cycling stability of the h-B<sub>10</sub>N<sub>12</sub> anode in the charging–discharging process, we evaluate the total volume change described as:

$$\Delta V = \frac{V_{\text{Na}} - V_0}{V_0} \times 100\% \quad (8)$$

where  $V_{\text{Na}}$ , and  $V_0$  are the volume of Na-adsorbed and empty h-B<sub>10</sub>N<sub>12</sub> structures, respectively. The sodiation behavior happens from the original empty system to the full one and desodiation is the inverse process. Therefore, the empty and full Na-adsorbed states of the h-B<sub>10</sub>N<sub>12</sub> anode are two boundary conditions. After calculation, we found the overall volume change of the h-B<sub>10</sub>N<sub>12</sub> anode to be  $2.77\%$ , which is much smaller than the experimental value of modified graphite ( $80\%$ )<sup>68</sup> and comparable to those of lz1-BN ( $2.23\%$ )<sup>26</sup> and 3D-Si<sub>2</sub>BN ( $2.7\%$ ).<sup>62</sup> This high cycling stability is attributed to the intrinsic ductility as well as the mechanical anisotropy that displays the axial-deformation resistance and radial flexibility.

For clarity, we summarize the key performance parameters of the h-B<sub>10</sub>N<sub>12</sub> anode in Table 2, and compare them with other previously reported systems for SIB anodes, including 3D boron nitrides,<sup>26,27</sup> boron-nitride-based anodes,<sup>61,62</sup> modified graphite,<sup>68</sup> Si<sub>24</sub>,<sup>69</sup> graphene-nanoribbon-based HZGM-42,<sup>70</sup> and silicene-nanoribbon-based ISN.<sup>67</sup> Furthermore, we also compare the metallicity, porosity, and ductility of h-B<sub>10</sub>N<sub>12</sub>, as well as its application as a SIB anode material, with some other boron nitrides (see Table S1, ESI<sup>†</sup>). These results show that h-B<sub>10</sub>N<sub>12</sub> is the first 3D metallic boron-nitride SIBs anode candidate that integrates all the advantages of ordered porosity, intrinsic metallicity, and mechanical ductility together, thus, leading to high theoretical capacity, excellent rate performance, and long cycling life.

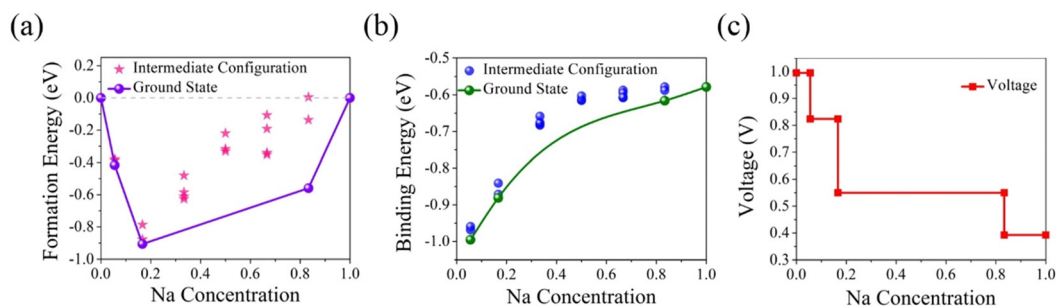


Fig. 5 (a) Formation energy and ground state hull of intermediate configurations, (b) binding energy curve and (c) voltage profile of most stable states of h-B<sub>10</sub>N<sub>12</sub>.

Table 2 Comparison of the key performance parameters of h-B<sub>10</sub>N<sub>12</sub> with some other reported representative anode materials for SIBs

Structure	Specific capacity (mA h g <sup>-1</sup> )	Diffusion barrier (eV)	Average open-circuit voltage (V)	Volume change (%)	Mechanical feature	Electronic property
h-B <sub>10</sub> N <sub>12</sub> [this work]	582.21	0.06–0.12	0.58	2.77	Ductile	Metallic
lz1-BN <sup>26</sup>	539.94	0.27	0.33	2.23	Brittle	Semiconducting
3D-B <sub>2</sub> N <sub>2</sub> <sup>27</sup>	599.90	0.04–0.08	0.13	0.96	Ductile	Semiconducting
h-BC <sub>2</sub> N <sup>61</sup>	549.00	0.35	0.31	0.03	Ductile	Semiconducting
3D-Si <sub>2</sub> BN <sup>62</sup>	341.61	0.19–0.21	0.15	2.70	Brittle	Semiconducting
Modified graphite <sup>10,68</sup>	109	0.40	0.66	80	Ductile	Metallic
Si <sub>24</sub> <sup>69,71</sup>	159	0.68	0.30	2.30	Ductile	Metallic
HZGM-42 <sup>70</sup>	318.5	0.08	0.43	1.85	Brittle	Semi-metallic
ISN <sup>67</sup>	159.5	0.005	1.35	2.80	Ductile	Semi-metallic

## 4. Conclusions

In summary, unlike the widely studied boron nitrides, we propose a new 3D porous and metallic boron nitride allotrope named h-B<sub>10</sub>N<sub>12</sub> for the anode of SIBs. H-B<sub>10</sub>N<sub>12</sub> is ductile and dynamically, thermally and mechanically stable, exhibiting resistance to deformation, especially in the axial direction due to the orderly arrangement of the B–B and N–N dimers. The calculated results of the electronic band structure show that h-B<sub>10</sub>N<sub>12</sub> is metallic, and a subsequent TB model analysis indicates that the metallicity originates from the synergistic contribution of the p-orbital of sp<sup>2</sup>-hybridized B and N atoms. More importantly, h-B<sub>10</sub>N<sub>12</sub> is found to possess high reversible theoretical capacities of 582.21 mA h g<sup>-1</sup> in gravimetric and 663.72 mA h cm<sup>-3</sup> in volumetric densities, low diffusion barriers in the range of 0.06 to 0.12 eV, a small volume change of 2.77%, and a reasonable average open-circuit voltage of 0.58 V when used as an anode material. These results are due to its unique porous and ductile structure as well as the existence of conducting channels. The superior performance parameters imply that h-B<sub>10</sub>N<sub>12</sub> is a promising candidate material for SIB anodes. Our research expands the boron nitride family with new characteristics for SIB applications and broadens research perspectives to design boron nitrides with desirable properties in the future.

## Data availability

The data supporting this article have been included as part of the ESI.†

## Conflicts of interest

There are no conflicts to declare.

## Acknowledgements

This work is partially supported by the grant from the National Natural Science Foundation of China (Grants No. NSFC-12274007). It is also supported by the high-performance computing platform of Peking University, China. P. J. acknowledges partial support by the U.S. Department of Energy, Office of Basic Energy Sciences, Division of Materials Sciences and Engineering under award DE-FG02-96ER45579.

## References

- J. Deng, C. Bae, A. Denlinger and T. Miller, Electric vehicles batteries: Requirements and challenges, *Joule*, 2020, **4**, 511–515.
- M. Weiss, R. Ruess, J. Kasnatscheew, Y. Levartovsky, N. R. Levy, P. Minnmann, L. Stolz, T. Waldmann, M. Wohlfahrt-Mehrens, D. Aurbach, M. Winter, Y. Ein-Eli and J. Janek, Fast charging of lithium-ion batteries: A review of materials aspects, *Adv. Energy Mater.*, 2021, **11**, 2101126.
- H. Ye, S. Xin, Y.-X. Yin and Y.-G. Guo, Advanced porous carbon materials for high-efficient lithium metal anodes, *Adv. Energy Mater.*, 2017, **7**, 1700530.
- R. A. Adams, A. Varma and V. G. Pol, Carbon anodes for nonaqueous alkali metal-ion batteries and their thermal safety aspects, *Adv. Energy Mater.*, 2019, **9**, 1900550.
- J. Liu, T. Zhao, S. Zhang and Q. Wang, A new metallic carbon allotrope with high stability and potential for lithium ion battery anode material, *Nano Energy*, 2017, **38**, 263–270.
- D. Ni, Y. Shen, Y. Shen, Q. Wang, Y. Kawazoe and P. Jena, Hex-C<sub>558</sub>: A new porous metallic carbon allotrope for lithium-ion battery anode, *Carbon*, 2021, **183**, 652–659.
- M. M. Obeid and Q. Sun, Assembling biphenylene into 3D porous metallic carbon allotrope for promising anode of lithium-ion batteries, *Carbon*, 2022, **188**, 95–103.
- H. Xie, Y. Qie, I. Muhammad and Q. Sun, B<sub>4</sub> cluster-based 3D porous topological metal as an anode material for both Li- and Na-ion batteries with a superhigh capacity, *J. Phys. Chem. Lett.*, 2021, **12**, 1548–1553.
- I. Muhammad, U. Younis, H. Xie, A. A. Khan, A. Khaliq, A. Samad, U. Schwingenschlöggl and Q. Sun, Borophene-based three-dimensional porous structures as anode materials for alkali metal-ion batteries with ultrahigh capacity, *Chem. Mater.*, 2021, **33**, 2976–2983.
- H. Hou, X. Qiu, W. Wei, Y. Zhang and X. Ji, Carbon anode materials for advanced sodium-ion batteries, *Adv. Energy Mater.*, 2017, **7**, 1602898.
- X. Li, F. Sun, H. Yan, Y. Wang, Y. Liang and F. Wu, Fluorinated boron nitride nanosheet as a high-performance electrode material for ion batteries via first-principles calculations, *J. Phys. Chem. Solids*, 2024, **190**, 112001.
- P. Das, B. Ball and P. Sarkar, Theoretical investigation of a tetrazine based covalent organic framework as a promising

- anode material for sodium/calcium ion batteries, *Phys. Chem. Chem. Phys.*, 2022, **24**, 21729–21739.
- 13 A. Ghosh, S. Pal and P. Sarkar, Rational design of two-dimensional porous boron phosphide as efficient cathode material for Li and Na ion batteries: A first-principles study, *J. Phys. Chem. C*, 2022, **126**, 5092–5100.
  - 14 W. Zhou, H. Xie, S. Wang, Q. Wang and P. Jena, A 3D porous honeycomb carbon as Na-ion battery anode material with high capacity, excellent rate performance, and robust stability, *Carbon*, 2020, **168**, 163–168.
  - 15 S. Li, Y. Shen, D. Ni and Q. Wang, A new 3D metallic carbon allotrope composed of penta-graphene nanoribbons as a high-performance anode material for sodium-ion batteries, *J. Mater. Chem. A*, 2021, **9**, 23214–23222.
  - 16 M. M. Obeid, D. Ni, P.-H. Du and Q. Sun, Design of three-dimensional metallic biphenylene networks for Na-ion battery anodes with a record high capacity, *ACS Appl. Mater. Interfaces*, 2022, **14**, 32043–32055.
  - 17 N. Izyumskaya, D. O. Demchenko, S. Das, Ü. Özgür, V. Avrutin and H. Morkoç, Recent development of boron nitride towards electronic applications, *Adv. Electron. Mater.*, 2017, **3**, 1600485.
  - 18 J. D. Caldwell, I. Aharonovich, G. Cassabois, J. H. Edgar, B. Gil and D. N. Basov, Photonics with hexagonal boron nitride, *Nat. Rev. Mater.*, 2019, **4**, 552–567.
  - 19 G. Li, M. Zhu, W. Gong, R. Du, A. Eychemüller, T. Li, W. Lv and X. Zhang, Boron nitride aerogels with super-flexibility ranging from liquid nitrogen temperature to 1000 °C, *Adv. Funct. Mater.*, 2019, **29**, 1900188.
  - 20 S. Zhang, Q. Wang, Y. Kawazoe and P. Jena, Three-dimensional metallic boron nitride, *J. Am. Chem. Soc.*, 2013, **135**, 18216–18221.
  - 21 J. Dai, X. Wu, J. Yang and X. C. Zeng, Unusual metallic microporous boron nitride networks, *J. Phys. Chem. Lett.*, 2013, **4**, 3484–3488.
  - 22 H. Wang, W. Zhang and P. Huai, Novel 3D metallic boron nitride containing only sp<sup>2</sup> bonds, *J. Phys. D: Appl. Phys.*, 2017, **50**, 385302.
  - 23 M. Xiong, K. Luo, Y. Pan, L. Liu, G. Gao, D. Yu, J. He, B. Xu and Z. Zhao, Hard three-dimensional BN framework with one-dimensional metallicity, *J. Alloys Compd.*, 2018, **731**, 364–368.
  - 24 B. Li, K. Luo, J. Chen, C. Xie, Y. Gao, L. Zhu, Q. Huang, M. Ma, Y. Zhang, Z. Zhao, J. He and Y. Tian, Design of a series of metallic B<sub>x</sub>N<sub>x+1</sub> with tunable mechanical properties, *J. Phys. Chem. Lett.*, 2021, **12**, 1979–1984.
  - 25 Y. Shen, H. Xie and Q. Wang, Pentagonal B<sub>2</sub>N<sub>3</sub>-based 3D metallic boron nitride with high energy density, *J. Phys.: Condens. Matter*, 2021, **33**, 165702.
  - 26 N. Khossossi, D. Singh, W. Luo and R. Ahuja, Flexible 3D porous boron nitride interconnected network as a high-performance Li-and Na-ion battery electrodes, *Electrochim. Acta*, 2022, **421**, 140491.
  - 27 X. Lin, H. Lin and Y. Huang, Three-dimensional porous diboron dinitride as a high-performance anode material for sodium/potassium-ion batteries: A first principles study, *ChemistrySelect*, 2023, **8**, e202300719.
  - 28 G. Kresse and J. Furthmüller, Efficient iterative schemes for *ab initio* total-energy calculations using a plane-wave basis set, *Phys. Rev. B: Condens. Matter Mater. Phys.*, 1996, **54**, 11169–11186.
  - 29 P. E. Blöchl, Projector augmented-wave method, *Phys. Rev. B: Condens. Matter Mater. Phys.*, 1994, **50**, 17953–17979.
  - 30 G. Kresse and D. Joubert, From ultrasoft pseudopotentials to the projector augmented-wave method, *Phys. Rev. B: Condens. Matter Mater. Phys.*, 1999, **59**, 1758–1775.
  - 31 M. P. Teter, M. C. Payne and D. C. Allan, Solution of Schrödinger's equation for large systems, *Phys. Rev. B: Condens. Matter Mater. Phys.*, 1989, **40**, 12255–12263.
  - 32 J. P. Perdew, K. Burke and M. Ernzerhof, Generalized gradient approximation made simple, *Phys. Rev. Lett.*, 1996, **77**, 3865–3868.
  - 33 J. Heyd, G. E. Scuseria and M. Ernzerhof, Hybrid functionals based on a screened Coulomb potential, *J. Chem. Phys.*, 2003, **118**, 8207–8215.
  - 34 J. Heyd, G. E. Scuseria and M. Ernzerhof, Erratum: “Hybrid functionals based on a screened Coulomb potential” [*J. Chem. Phys.* 118, 8207 (2003)], *J. Chem. Phys.*, 2006, **124**, 219906.
  - 35 H. J. Monkhorst and J. D. Pack, Special points for Brillouin-zone integrations, *Phys. Rev. B*, 1976, **13**, 5188–5192.
  - 36 K. Parlinski, Z. Q. Li and Y. Kawazoe, First-principles determination of the soft mode in cubic ZrO<sub>2</sub>, *Phys. Rev. Lett.*, 1997, **78**, 4063–4066.
  - 37 A. Togo and I. Tanaka, First principles phonon calculations in materials science, *Scr. Mater.*, 2015, **108**, 1–5.
  - 38 D. Bucher, L. C. T. Pierce, J. A. McCammon and P. R. L. Markwick, On the use of accelerated molecular dynamics to enhance configurational sampling in *ab initio* simulations, *J. Chem. Theory Comput.*, 2011, **7**, 890–897.
  - 39 D. Evans and B. Holian, The Nose-Hoover thermostat, *J. Chem. Phys.*, 1985, **83**, 4069–4074.
  - 40 S. H. Zhang and R. F. Zhang, AELAS: Automatic ELAStic property derivations via highthroughput first-principles computation, *Comput. Phys. Commun.*, 2017, **220**, 403–416.
  - 41 A. A. Mostofi, J. R. Yates, Y.-S. Lee, I. Souza, D. Vanderbilt and N. Marzari, wannier90: A tool for obtaining maximally-localised Wannier functions, *Comput. Phys. Commun.*, 2008, **178**, 685–699.
  - 42 S. Grimme, Semiempirical GGA-type density functional constructed with a long-range dispersion correction, *J. Comput. Chem.*, 2006, **27**, 1787–1799.
  - 43 G. Mills and H. Jónsson, Quantum and thermal effects in H<sub>2</sub> dissociative adsorption: Evaluation of free energy barriers in multidimensional quantum systems, *Phys. Rev. Lett.*, 1994, **72**, 1124–1127.
  - 44 J. M. L. Martin, J. El-Yazal, J. François and R. Gijbels, The structure and energetics of B<sub>3</sub>N<sub>2</sub>, B<sub>2</sub>N<sub>3</sub>, and BN<sub>4</sub>, *Mol. Phys.*, 1995, **85**, 527–537.
  - 45 J. Li, X. Fan, Y. Wei and G. Chen, Penta-B<sub>x</sub>N<sub>y</sub> sheet: a density functional theory study of two-dimensional material, *Sci. Rep.*, 2016, **6**, 31840.
  - 46 M. Amiri, J. Beheshtian, F. Shayeganfar, M. Faghihnasiri, R. Shahsavari and A. Ramazani, Electro-optical properties

- of, onolayer and bilayer pentagonal BN: First principles study, *Nanomaterials*, 2020, **10**, 440.
- 47 H. Zheng, H. Bu and L. Sun, Predicting the structural, electronic and mechanical properties of three-dimensional boron nitride foam containing sp, sp<sup>2</sup> and sp<sup>3</sup> hybridized bonds, *J. Phys.: Conf. Ser.*, 2019, **1213**, 042022.
  - 48 S. Kawai, O. Krejčí, T. Nishiuchi, K. Sahara, T. Kodama, R. Pawlak, E. Meyer, T. Kubo and A. S. Foster, Three-dimensional graphene nanoribbons as a framework for molecular assembly and local probe chemistry, *Sci. Adv.*, 2020, **6**, eaay8913.
  - 49 F. Mouhat and F.-X. Coudert, Necessary and sufficient elastic stability conditions in various crystal systems, *Phys. Rev. B: Condens. Matter Mater. Phys.*, 2014, **90**, 224104.
  - 50 Z.-J. Wu, E.-J. Zhao, H.-P. Xiang, X.-F. Hao, X.-J. Liu and J. Meng, Crystal structures and elastic properties of superhard IrN<sub>2</sub> and IrN<sub>3</sub> from first principles, *Phys. Rev. B: Condens. Matter Mater. Phys.*, 2007, **76**, 054115.
  - 51 R. Hill, The elastic behaviour of a crystalline aggregate, *Proc. Phys. Soc., London, Sect. A*, 1952, **65**, 349–354.
  - 52 V. A. Gorodtsov and D. S. Lisovenko, Extreme values of Young's modulus and Poisson's ratio of hexagonal crystals, *Mech. Mater.*, 2019, **134**, 1–8.
  - 53 S. F. Pugh, XCII. Relations between the elastic moduli and the plastic properties of polycrystalline pure metals, *London, Edinburgh Dublin Philos. Mag. J. Sci.*, 1954, **45**, 823–843.
  - 54 J. Dai, X. Wu, J. Yang and X. C. Zeng, Porous boron nitride with tunable pore size, *J. Phys. Chem. Lett.*, 2014, **5**, 393–398.
  - 55 W. Sun, D. Ni and Q. Wang, PHP-graphene nanoribbon-assembled porous metallic carbon for sodium-ion battery anode with high specific capacity, *Carbon*, 2023, **202**, 112–118.
  - 56 W. Sun, D. Ni, C. Hou, Q. Wang, Y. Kawazoe and P. Jena, A new 3D porous metallic carbon allotrope composed of 5-7 nanoribbons as an anode material for sodium-ion batteries, *J. Power Sources*, 2023, **584**, 233594.
  - 57 A. D. Becke and K. E. Edgecombe, A simple measure of electron localization in atomic and molecular systems, *J. Chem. Phys.*, 1990, **92**, 5397–5403.
  - 58 W. Tang, E. Sanville and G. Henkelman, A grid-based Bader analysis algorithm without lattice bias, *J. Phys.: Condens. Matter*, 2009, **21**, 084204.
  - 59 C. Yang, X. Sun, X. Zhang, J. Li, J. Ma, Y. Li, L. Xu, S. Liu, J. Yang, S. Fang, Q. Li, X. Yang, F. Pan, J. Lu and D. Yu, Is graphite nanomesh a promising anode for the Na/K-Ions batteries?, *Carbon*, 2021, **176**, 242–252.
  - 60 S. Komaba, W. Murata, T. Ishikawa, N. Yabuuchi, T. Ozeki, T. Nakayama, A. Ogata, K. Gotoh and K. Fujiwara, Electrochemical Na insertion and solid electrolyte interphase for hard-carbon electrodes and application to Na-ion batteries, *Adv. Funct. Mater.*, 2011, **21**, 3859–3867.
  - 61 L. Li, X. Li, X. Li, H. Chen, H. Liu, J. Chen and Y. Zhang, Three-dimensional porous h-BC<sub>2</sub>N based on BN chains and prismane C<sub>8</sub> units for alkali metal ion battery anodes, *J. Phys. Chem. Lett.*, 2022, **13**, 2348–2355.
  - 62 U. Younis, I. Muhammad, W. Wu, S. Ahmed, Q. Sun and P. Jena, Assembling Si<sub>2</sub>BN nanoribbons into a 3D porous structure as a universal anode material for both Li- and Na-ion batteries with high performance, *Nanoscale*, 2020, **12**, 19367–19374.
  - 63 C. Uthaisar and V. Barone, Edge effects on the characteristics of Li diffusion in graphene, *Nano Lett.*, 2010, **10**, 2838–2842.
  - 64 S. P. Ong, W. D. Richards, A. Jain, G. Hautier, M. Kocher, S. Cholia, D. Gunter, V. L. Chevrier, K. A. Persson and G. Ceder, Python Materials Genomics (pymatgen): A robust, open-source python library for materials analysis, *Comput. Mater. Sci.*, 2013, **68**, 314–319.
  - 65 S. Wang, Q. Bai, A. M. Nolan, Y. Liu, S. Gong, Q. Sun and Y. Mo, Lithium chlorides and bromides as promising solid-state chemistries for fast ion conductors with good electrochemical stability, *Angew. Chem., Int. Ed.*, 2019, **58**, 8039–8043.
  - 66 Y. Qie, J. Liu, S. Wang, Q. Sun and P. Jena, Tetragonal C24: A topological nodal-surface semimetal with potential as an anode material for sodium ion batteries, *J. Mater. Chem. A*, 2019, **7**, 5733–5739.
  - 67 Y. Qie, J. Liu, X. Li, S. Wang, Q. Sun and P. Jena, Interpenetrating silicene networks: A topological nodal-line semimetal with potential as an anode material for sodium ion batteries, *Phys. Rev. Mater.*, 2018, **2**, 084201.
  - 68 Z. Xu, G. Yoon, K. Park, H. Park, O. Tamwattana, S. J. Kim, W. M. Seong and K. Kang, Tailoring sodium intercalation in graphite for high energy and power sodium ion batteries, *Nat. Commun.*, 2019, **10**, 2598.
  - 69 U. Arrieta, N. A. Katcho, O. Arcelus and J. Carrasco, First-principles study of sodium intercalation in crystalline Na<sub>x</sub>Si<sub>24</sub> (0 ≤ x ≤ 4) as anode material for Na-ion batteries, *Sci. Rep.*, 2017, **7**, 5350.
  - 70 Y. Shen, Q. Wang, Y. Kawazoe and P. Jena, Potential of porous nodal-line semi-metallic carbon for sodium-ion battery anode, *J. Power Sources*, 2020, **478**, 228746.
  - 71 D. Y. Kim, S. Stefanoski, O. O. Kurakevych and T. A. Strobel, Synthesis of an open-framework allotrope of silicon, *Nat. Mater.*, 2014, **14**, 169–173.